

## ARTICLE OPEN



# The corrosion mechanism of lead-glazed pottery in Han dynasty

Kexin Zhang<sup>1,2</sup>, Chen Wu<sup>3</sup>✉, Jing Zhao<sup>1</sup>✉, Wendi Yu<sup>1</sup> and Meng Zhao<sup>1,2</sup>

Ancient pottery, having endured prolonged burial in soil, invariably underwent the process of glaze corrosion. The micromorphology and structural composition of four lead-glazed pottery fragments dating back to the Han Dynasty, excavated in the Qinhan New Town within Xixian New area of Xi'an are elucidated by comprehensive analysis method. The results reveal that the corrosion products predominantly comprised  $\text{PbCO}_3$ ,  $\text{Pb}_3(\text{PO}_4)_2$ ,  $\text{CaCO}_3$ , and  $\text{Ca}_3(\text{PO}_4)_2$ . Concurrently, the presence of organic substances exhibiting characteristic self-excitation fluorescence in the cracks of the sample is identified through fluorescence microscopy and Fourier infrared spectroscopy. Through a comparative analysis of well-preserved and severely corroded samples, taking into account compositional analysis, observations of corrosion morphology, and the characteristics of corrosion products, it is deduced that the primary corrosion mechanisms involve chemical corrosion, microbial corrosion, and crack corrosion. This study provides a comprehensive depiction of glaze corrosion process inherent to lead-glazed pottery and establishes corresponding corrosion models.

*npj Materials Degradation* (2024)8:10; <https://doi.org/10.1038/s41529-024-00428-y>

## INTRODUCTION

Alkali-based vitreous glazes have a rich history spanning millennia within the annals of human civilization. Glass first appeared in the Near East and Egypt in the form of glazed stone and painted pottery. Glass first appeared in the Near East and Egypt in the form of glazed stone and painted pottery, these early glazes and glassworks prominently featured copper oxide as a primary colorant<sup>1</sup>. Notably, the inception of glazed pottery in Mesopotamia occurred roughly two millennia after the advent of glazed stone and painted pottery<sup>1,2</sup>. The development of pottery in ancient China is characterized by a rich heritage distinguished by noteworthy accomplishments. Glazed pottery made its debut in China prior to the establishment of the Shang Dynasty, evolving from the techniques employed in printed hard pottery. This advancement introduced a transformative feature: the application of a transparent glaze layer onto the ceramic matrix, known as high-fire glaze<sup>3,4</sup>. In contrast, China's low-fire lead-glazed pottery found its origins during the Warring States Period (475–221 BC) and subsequently experienced a period of significant prosperity during the Han Dynasty (202 BC–220 AD)<sup>4,5</sup>.

Glazed pottery exhibits inherent attributes of diminished chemical stability, low hardness, and limited adherence between the matrix and the glaze<sup>6</sup>. Over the protracted course of burial, the glaze of lead-glazed pottery has been susceptible to an array of maladies, encompassing the development of silver or gold covering layers, glaze detachment, and the emergence of alteration pitting<sup>7–9</sup>. Prior investigations into the corrosion phenomena affecting lead-glazed pottery have encompassed a diverse array of subjects. These inquiries have delved into facets such as glaze corrosion instigated by ion exchange mechanisms involving hydrogen ions and modifier ions (e.g.,  $\text{Na}^+$ ,  $\text{K}^+$ ,  $\text{Pb}^{2+}$ ) within glass network alongside the dissolution of the network itself, notably silica dissolution, within the burial environment<sup>10–13</sup>. Additionally, studies have explored the deposition of  $\text{PbCO}_3$ <sup>14–16</sup>

and phosphate<sup>17,18</sup> onto the lead-glazed surface under varying burial conditions, as well as the effects of colorants, including Cu and Fe, on the extent of corrosion of a lead glaze<sup>19–21</sup>. Simultaneously, scholarly investigations have revealed the capacity of microorganisms to induce corrosion phenomena on the surface of lead glaze. These microbial-induced effects encompass etching, pitting, leaching, discoloration, glass degradation, gel layer formation, etc.<sup>22–25</sup>.

In 2019, Xi'an Cultural Relics Conservation and Archaeology Institute initiated archaeological excavations within the region situated west of Qinhan Avenue, north of Zhangliang Road. 114 tombs dating from the middle and late Western Han Dynasty through to the Eastern Han Dynasty were brought to light through the excavation efforts. Consequently, the excavation yielded a remarkable assortment of 528 artifacts, comprising pottery, porcelain, metal wares and various utensils. Among these findings, glazed pottery, a quintessential funerary item of the Han Dynasty, was discovered within a multitude of tombs, each exhibiting distinct glaze colors and preservation conditions. These diverse discoveries serve as crucial empirical evidence for advancing the understanding of the corrosion mechanisms impacting Han Dynasty glazed pottery.

In the context of this study, four exemplary artifacts emerged: fragments of green lead-glazed pottery and yellow-green lead-glazed pottery. These artifacts were unearthed from three distinct tombs during the excavation phase, conducted between June and July 2019, at a depth ranging from 10 to 15 meters below the surface. Notably, the corrosion of these fragments is characterized by pronounced severity, manifesting as an irregular distribution of surface discoloration and the presence of white matter. It is noteworthy that QHXC-1 and QHXC-4 is attributed to the late Western Han Dynasty, while QHXC-2 and QHXC-3 represent pottery fragments originating from the middle and late periods of the Eastern Han Dynasty, respectively. The chemical composition

<sup>1</sup>Shanghai Institute of Ceramics, Chinese Academy of Sciences, 200050 Shanghai, China. <sup>2</sup>School of Materials and Chemistry, University of Shanghai for Science and Technology, 200093 Shanghai, China. <sup>3</sup>Xi'an Institute of Archaeology and Conservation on Cultural Heritage, 710068 Xi'an, China. ✉email: wuchen124@163.com; zhaojing@mail.sic.ac.cn

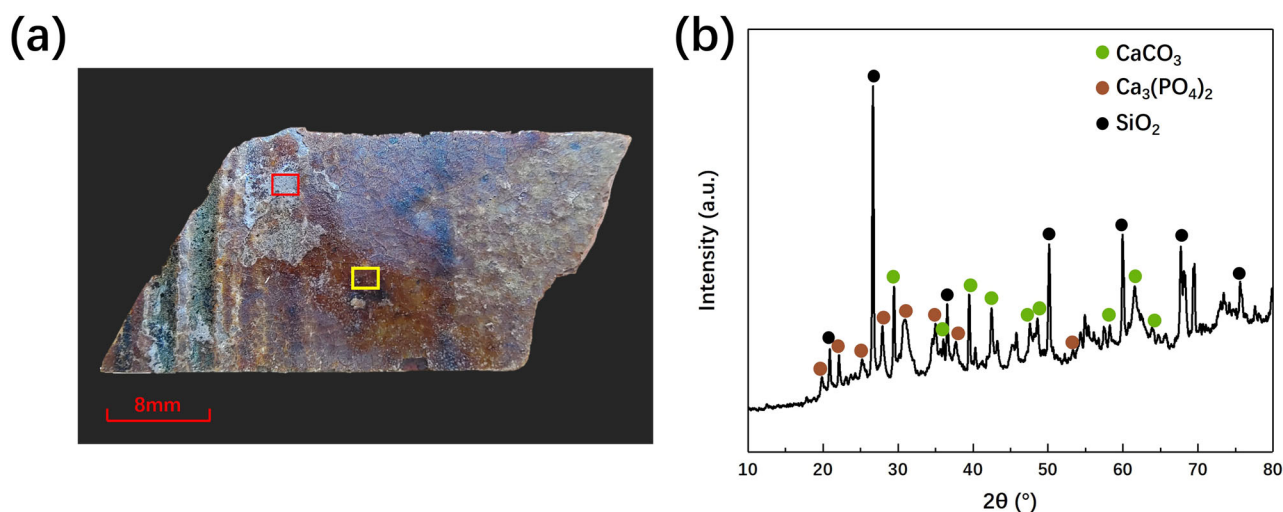


**Fig. 1** Optical image and XRD curve for QHXC-1. **a** Optical image, featuring white corrosion substance (highlighted in red box), subjected to analysis via XRD and XRF. Additionally, the well-preserved glaze area (highlighted in yellow box) was also analyzed using XRF. **b** XRD spectral curve of the red box area.

**Table 1.** Chemical composition of the marked positions in Fig. 1a (QHXC-1), Fig. 3a (QHXC-2), Fig. 5a (QHXC-3) and Fig. 7a (QHXC-4) (normalized wt%).

Element		Na	Mg	Al	Si	K	Ca	Ti	Fe	Cu	Pb	O	P	Mn	Ba	Sn
QHXC-1	corrosion	0.25	0.88	5.04	14.89	2.16	5.12	0.61	5.96	0.04	36.59	27.95	0.28	0.08		0.13
	well-preserved	0.05	0.60	2.43	8.03	0.24	0.84	0.19	2.29	0.05	71.54	13.41	0.13	0.03	0.02	0.14
QHXC-2	corrosion	0.10	0.28	0.53	2.28	0.13	6.80	0.05	0.33	1.21	71.76	11.57	4.09		0.04	0.02
	well-preserved			0.21	2.84		0.87	0.01	0.26	1.98	88.43	4.21	0.09	0.01	0.12	0.01
QHXC-3	corrosion		0.15	0.55	2.45		1.02	0.05	0.64	0.63	89.06	4.24		0.01	0.11	0.55
	well-preserved		0.12	0.39	1.06		0.97	0.04	0.42	0.33	93.34	2.36		0.01	0.14	0.29
QHXC-4	corrosion	0.54	1.13	2.46	11.47	0.53	4.46	0.22	2.70	0.25	56.58	19.40		0.04	0.01	0.06
	well-preserved	0.26	1.35	2.53	12.35	0.84	3.43	0.19	2.20	0.14	56.57	19.93		0.03	0.02	0.04

and micromorphological characteristics of the glaze corrosion in four untreated fragments were systematically examined and analyzed. This investigation was undertaken to gain insight into the corrosion phenomena and process in the burial environment. Within the scope of this study, a detailed exposition of the glaze corrosion progression inherent to lead-glazed pottery is offered and pertinent corrosion models are established. These research findings contribute to the advancement of scientific knowledge pertaining to the corrosion of ancient lead-glazed pottery. Furthermore, they furnish valuable scientific references for the effective preservation and safeguarding of excavated glazed pottery artifacts.

## RESULTS

### Analysis of composition, structure and morphology of samples

For the determination of corrosion products, surface elemental distribution and original glaze composition of the QHXC-1 artifact, a comprehensive analytical approach was adopted. Specifically, X-ray diffraction diffractometry (XRD) was employed to analyze the white corrosion area, delineated within the red box area of Fig. 1a. Concurrently, X-ray fluorescence spectroscopy (XRF) was utilized to assess the elemental composition of both the white corrosion area (red box area) and well-preserved glaze layer area (yellow box area) as illustrated in Fig. 1a. The detailed test results can be found in Table 1. Additionally, the XRD analysis outcomes unveiled the formation of  $\text{CaCO}_3$  and  $\text{Ca}_3(\text{PO}_4)_2$  on the surface of

the sample, alongside the presence of  $\text{SiO}_2$  within the substrate (Fig. 1b).

In order to comprehensively assess alterations within the glaze layer's elemental composition, a surface scan composition analysis was conducted on the sample cross-section situated within the delineated red box area of Fig. 2a, utilizing XRF surface scan mode. The investigation revealed a predominantly consistent distribution of Pb and Sn elements within the glaze layer, with P and Ca forming a composite elemental band at the transition region of the lead glaze layer, as depicted in Fig. 2b. Notably, these elements originate from the soil porewater and are primarily transported through cracks within the glaze layer, indicated by the red markings in Fig. 2b.

It is speculated that the formation of  $\text{Ca}_3(\text{PO}_4)_2$  is primarily a result of the interaction between P element in the soil and the calcium on the surface of the lead glaze, culminating in the creation of calcium phosphate. Furthermore, fluid migration from the surface towards the interior along the cracks in the glaze layer, culminated in the accumulation of P and Ca at the transition zone of the lead glaze. These elements subsequently diffused and dispersed within the matrix, as evidenced in Fig. 2. Simultaneously,  $\text{Ca}^{2+}$  ions at the surface of the lead glaze underwent chemical corrosion through carbonic acid from the soil, leading to the formation of  $\text{CaCO}_3$ .

The corrosion area on the surface of QHXC-2 green glaze can be divided into two parts: a compacted upper layer referred to as Z1 and a more porous sub-surface, designated as Z2, characterized by a reduced presence of corrosion substances. This distinction is visually demonstrated within the red box of Fig. 3a. Micro-area

XRD was employed to assess the corrosion substances on the surface of Z1, revealing the presence of lead phosphate and lead carbonate.

Elemental composition analyses of both Z1 and Z2 were conducted using XRF, with the findings detailed in Table 1. Employing XRF surface scan mode, the composition analysis was extended to the area within the red box area outlined in Fig. 4a. This analysis revealed that the distribution patterns of Pb, Sn and Cu elements mirrored those observed in QHXC-1. Additionally, the distribution of Ca and P elements was prominent in the outermost layer, Z1. Furthermore, it was noted that the outermost layer

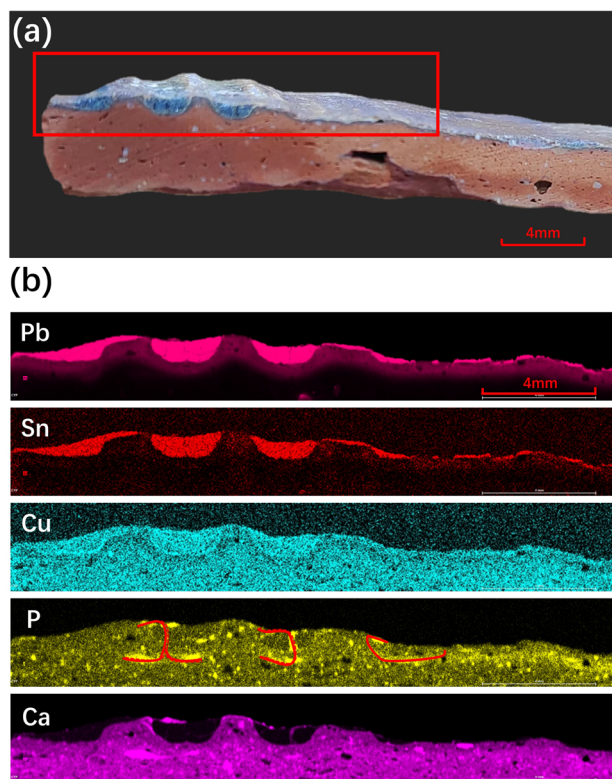


**Fig. 2** Optical images and XRF test results for QHXC-1. **a** Optical image and XRF test area (red box). **b** Element distribution images (with brighter color signifying higher element, the same below).

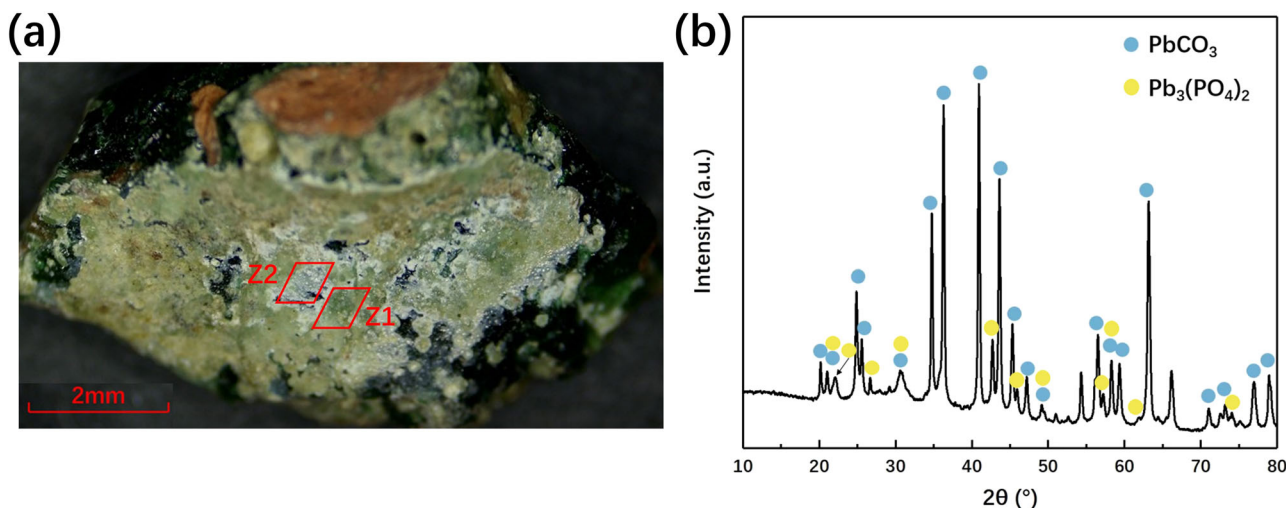


**Fig. 3** Optical images and XRD spectral curve for QHXC-2. **a** Optical image; compacted surface Z1 was analyzed via both XRD and XRF; and the more porous sub-surface Z2 underwent XRF analysis. **b** XRD spectral curve derived from the Z1 area.

exhibited a higher concentration of structural elements such as Si and Al in comparison to the Z2 layer (Fig. 4).

The green glaze surface of the QHXC-3 sample exhibited the presence of brown corrosion substances (as depicted in red box area of Fig. 5a). To identify these substances, XRD analysis was conducted, confirming their primary composition as lead carbonate (as illustrated in Fig. 5b). In addition, XRF was used to assess the element composition content within the brown corrosion substances (red box area of Fig. 5a) and well-preserved glaze area of the QHXC-3 sample (yellow box area of Fig. 6a), and the test results are shown in Table 1. Furthermore, the composition distribution of the glaze section of the sample was analyzed using XRF surface scan mode. Figure 6, reveals a consistent distribution pattern for Pb, Sn and Cu. Specifically, Pb and Sn elements exhibited heightened concentrations on the outermost surface of the lead glaze layer, while the Cu element was primarily concentrated within the interior of the lead glaze. Apart from that, P elements were found to be scattered throughout the glaze layer.

The QHXC-4 glaze exhibited an overall glassy luster, with relatively good preservation. However, there is noticeable unevenness in the glaze color. XRF surface scanning results revealed an enrichment of Si, Al and Fe elements in the darker brown areas (Fig. 7b). In comparison to the original green glaze surface (green box area in Fig. 7a), the brown area showed an increase of Fe and Cu contents (yellow box area in Fig. 7a) from 2.20% and 0.19% to 2.70% and 0.22%, respectively. FurCa elements were sporadically scattered in the corrosion pits of the glaze.

#### Microstructure of the corroded area

Observations of particle-level alterations within the glaze and corrosion layers of QHXC-1 and QHXC-3 samples were conducted at the atomic scale utilizing transmission electron microscopy (TEM). Additionally, a comparative analysis of the microscopic morphology between QHXC-1 and QHXC-3 samples was undertaken<sup>26</sup>, the findings pertaining are shown in Fig. 8.

In the case of QHXC-1, the glaze layer's crystallinity exhibited superior characteristics, featuring discernible crystal lattice stripes (as depicted in Fig. 8a). Conversely, within the corrosion area (as depicted in Fig. 8b), the crystallinity degree deteriorated, accompanied by ion vacancy precipitation and structural alterations within the glaze layer. In contrast, the primary glaze layer of QHXC-3 displayed crystal sizes ranging from 200 to 300 nm in diameter (as depicted in Fig. 8c), whereas the lead carbonate

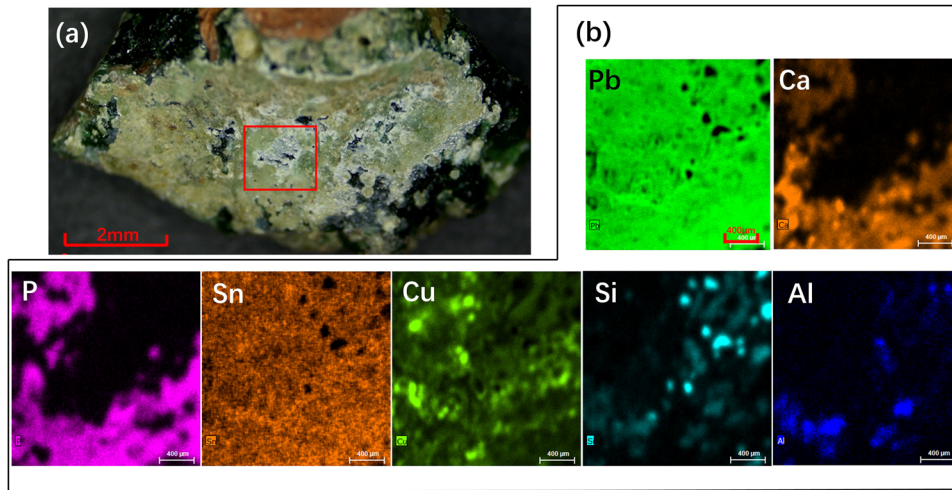


**Fig. 4** Optical image and XRF surface scan mode test results for QHXC-2. **a** Optical image and XRF test area (red box). **b** Element distribution images.

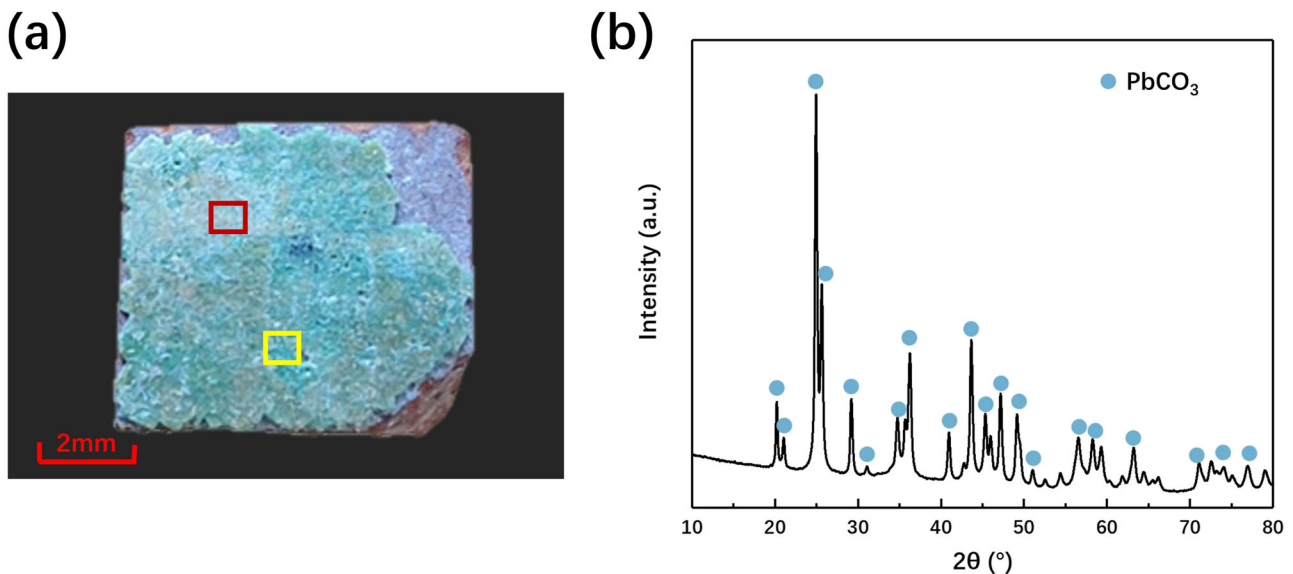


**Fig. 5** Optical image and XRD curve for QHXC-3. **a** Optical image; brown corrosion substances (red box) were subjected to the analysis via both XRD and XRF; well-preserved glaze area (yellow box) was analyzed via XRF. **b** XRD spectral curve of red box.

formations were approximately 100 nm in size (as depicted in Fig. 8d).

To facilitate a comprehensive comparative analysis of the varied morphologies of corrosion products, the extensively corroded QHXC-1 and QHXC-3 samples, along with the well-preserved QHXC-4 samples, underwent examination using scanning electron microscopy equipped with energy-dispersive X-ray spectroscopy (SEM-EDX) for backscattering and secondary electron imaging. The analysis revealed distinct surface corrosion patterns within the QHXC-1 samples, manifesting as three distinct types: lamellar petal-shaped corrosion, as depicted in Fig. 9b; regularly shaped conical columnar corrosion, illustrated in Fig. 9d; and curly plate columnar corrosion, shown in Fig. 9f.

Furthermore, the EDX test results, outlined in Table 2 provided additional insights. Specifically, P1 exhibited notably high concentrations of C and Fe elements, constituting 21.88% and 7.96%, respectively. Meanwhile, P2 displayed lower levels of C and Fe, at 17.78% and 13.41%, respectively, compared to P3, where cone-columnar or plate-columnar  $\text{PbCO}_3$  crystals had formed.

Regarding the fracture surface of the glaze layer within the QHXC-1 sample, a crack propagation under the influence of corrosion is evident, as depicted in Fig. 10a. Within these cracks, a diverse array of materials exhibits distinct distributions and morphologies. Notably, the upper portion of the crack, denoted as P4, exhibits the formation resembling clusters of flowers, as illustrated in Fig. 10b. Conversely, the inner corrosion area labeled as P5 manifests a lamellar petal-like formation, as depicted in Fig. 10c. Both regions contain a noticeable presence of P.

SEM-EDX employed to conduct an in-depth analysis of the backscattering and secondary electron imaging of the QHXC-3 sample. The EDX test results, providing valuable insights, are presented in Table 2. Notably, various corrosion pits with distinct morphologies were observed on the corroded green glaze surface of the QHXC-3 sample. Among these, discontinuous corrosion holes were prominently visible on the surface, as exemplified in Fig. 11c. Additionally, it was observed that the carbon content within the corrosion pits depicted in Fig. 11a was marginally lower than that in Fig. 11c. However, the content of Pb was higher in the latter.

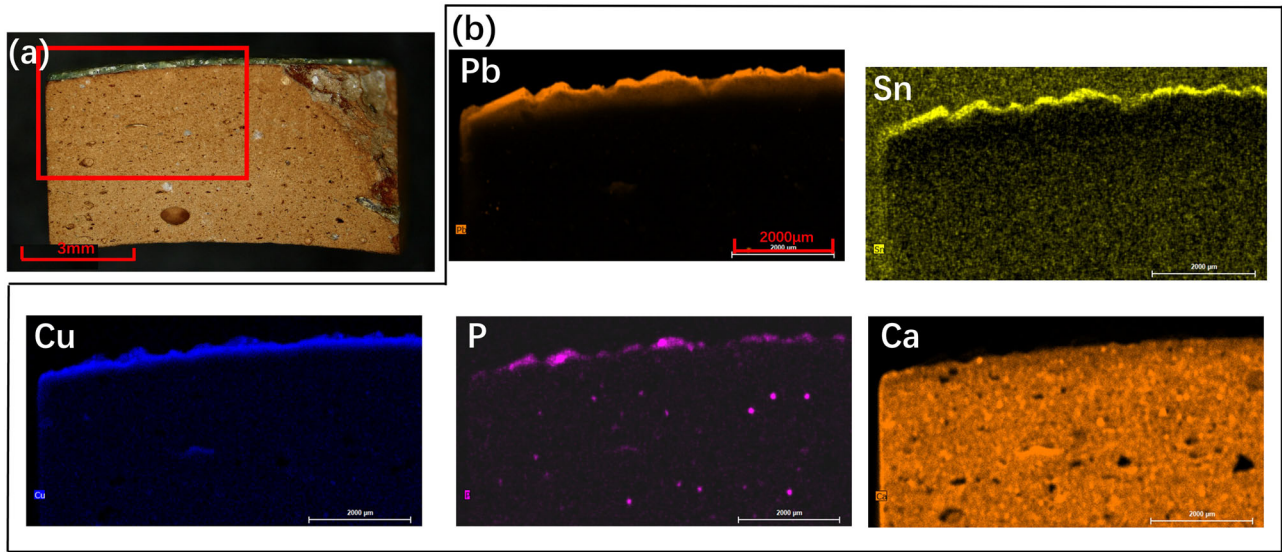


**Fig. 6** Optical photo and XRF surface scan mode test results for QHXC-3. **a** Optical photo and XRF test area. **b** Element distribution images in the test area.

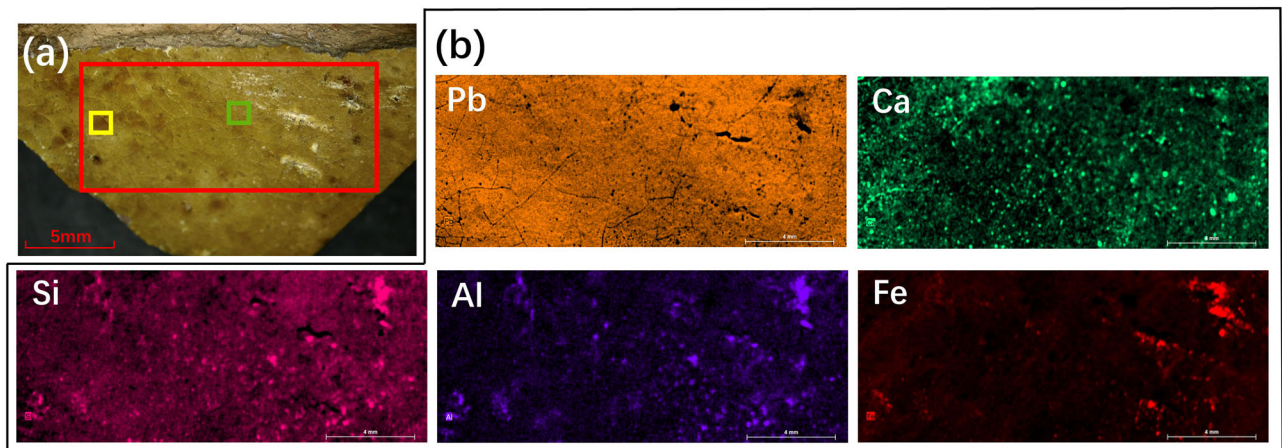


**Fig. 7** Optical photo and XRF surface scan mode test results for QHXC-4. **a** Optical photo and XRF test area. **b** Element distribution images within the designated test area.

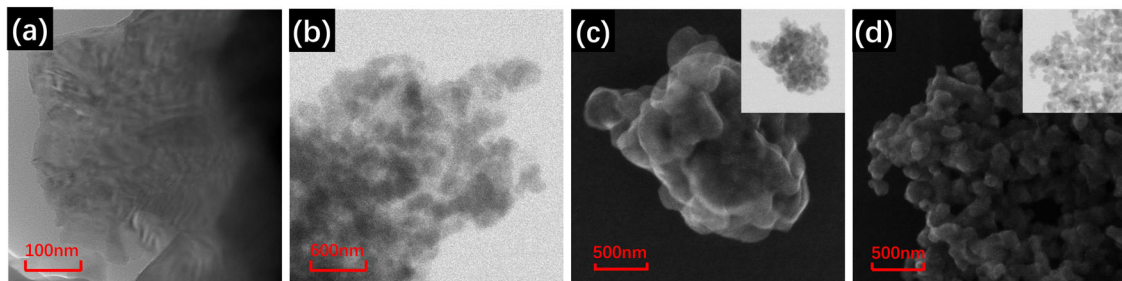


**Fig. 8** TEM results of QHXC-1 and QHXC-3. **a** Well-preserved glaze of QHXC-1. **b** Corroded glaze of QHXC-1. **c** Well-preserved glaze of QHXC-3. **d** Corroded glaze of QHXC-3.

Regarding the fracture surface of the glaze layer within the QHXC-3 sample, it was observed that hemispherical adherent deposits, containing 7–8% C element, had accumulated at both the glaze layer section and the glaze interface, as shown in Fig. 12a. These deposits exhibited particle diameters in the range of approximately 10–20 nm. Upon comparing the morphological

features and elemental composition of the surfaces and cross-sections of both QHXC-1 and QHXC-3 samples, it is found that there was a high content of C within the corroded samples. Notably, the regions labeled as P5, characterized by the formation of lamellar petal-like structures within the crack of QHXC-1 samples, exhibited the highest C content.

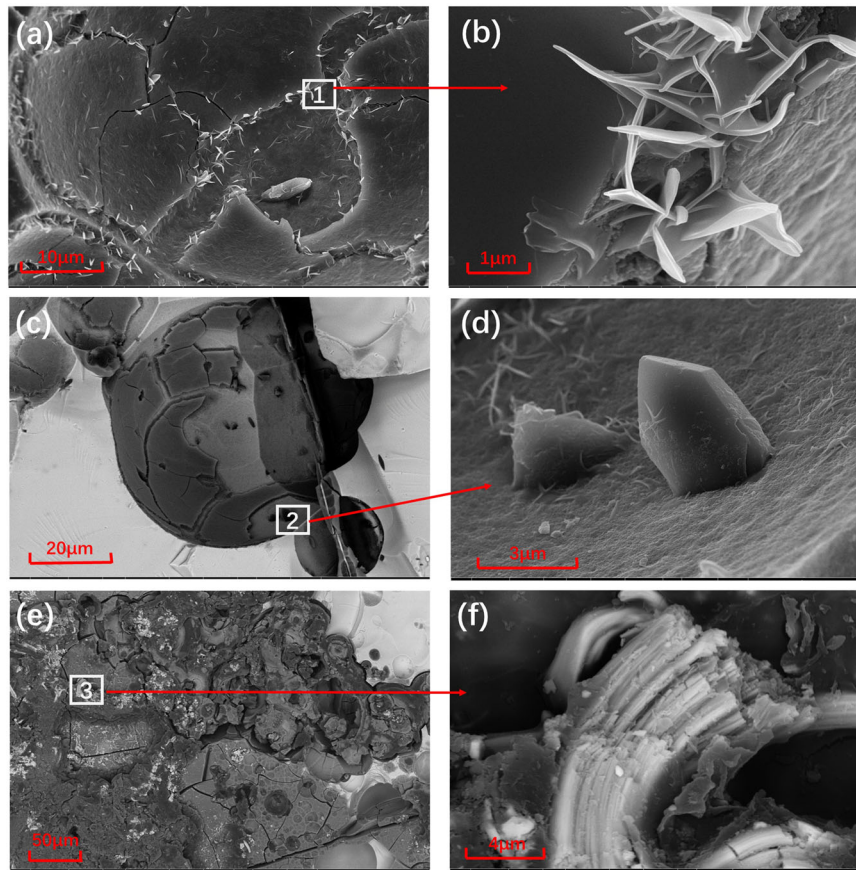


**Fig. 9** SEM images of enamel corrosion area on QHXC-1 surface. **a, b** Lamellar petal-shaped corrosion. **c, d** Regular cone columnar corrosion. **e, f** Curly plate columnar corrosion.

**Table 2.** Element composition in different area positions of QHXC-1 surface (P1-P3), QHXC-1 section (P4, P5), QHXC-3 surface (P6, P7) and QHXC-3 section (P8, P9) (normalized wt%).

Element	C	O	Mg	Al	Si	P	S	Cl	Ca	Fe	Pb
P1	21.88	16.39	0.44	1.85	7.17		1.17		1.16	7.96	41.74
P2	17.77	28.82		2.28	6.72		1.21			13.41	29.79
P3	13.67	18.38		0.61	2.22	0.60	1.20		0.75		62.57
P4	5.94	45.73	0.94	5.97	14.94	1.63			2.11	2.52	20.22
P5	38.99	9.29	0.22	2.55	8.09	2.84	0.89	0.76	3.20	3.59	28.88
P6	10.44	13.95				0.44	1.57		0.71		72.88
P7	18.14	19.32		0.23	0.62	0.48	1.02		1.46		58.73
P8	8.02	21.34		0.50	2.48		1.47		0.81		65.37
P9	7.12	20.62		0.61	2.36	0.80	1.68		0.74		66.07

Various depths of pits were observed on the glaze surface of QHXC-4 (Fig. 13a), with no apparent corrosion products detected within the glaze cracks. EDX surface scanning results of QHXC-4 indicated the loss of Si and Pb within the pits, while the corrosion products exhibited elevated levels of Ca, Mg and C (Fig. 13b).

#### Microfluorescence analysis of sample surface

In consideration of the potential influence of soil microbes on the surface of lead glaze prior to the excavation of the cultural relic samples, an examination of the bioluminescence effect on the surface of samples was conducted using an inverted fluorescence

phase contrast microscope (FL). This analysis involved the application of excitation light of blue (395 nm), green (470 nm) and red (545 nm), with the findings shown in Fig. 14. Remarkably, almost no fluorescence imagery was captured in the case of QHXC-2, which exhibited an absence of cracks (Fig. 14b). In contrast, the well-preserved glaze of QHXC-4 showed nonuniformity point-like weak fluorescence (Fig. 14d). The green copper-containing surfaces and severely corroded areas of both QHXC-1 and QHXC-3 samples showed relatively strong fluorescence effects (Fig. 14a, c), which mainly concentrated in the cracks of the glaze layer to form a distinctive ring-shaped fluorescence pattern. These fluorescence-emitting substances have the characteristic of

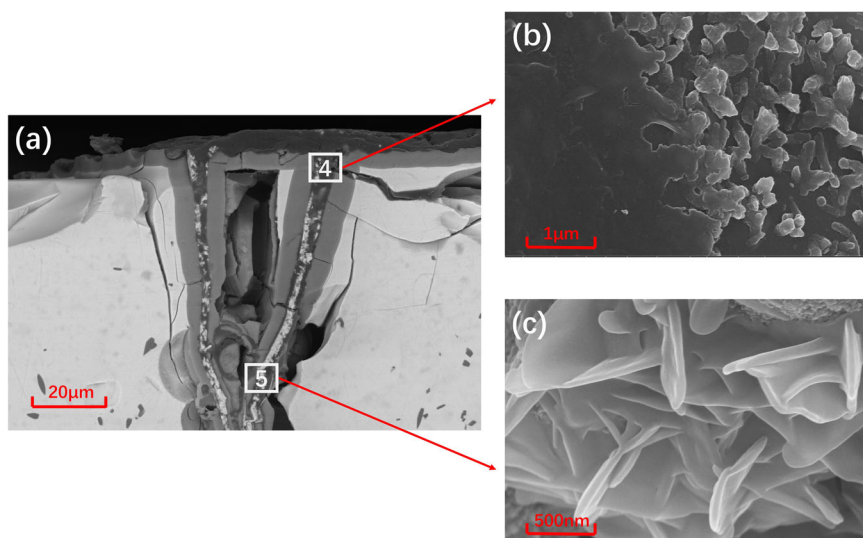


**Fig. 10 SEM images of cross-section of QHXC-1 glaze layer. a** Glaze cross-section crack. **b** Corrosion in the shape of clusters of flowers. **c** Corrosion in the shape of lamella petals.

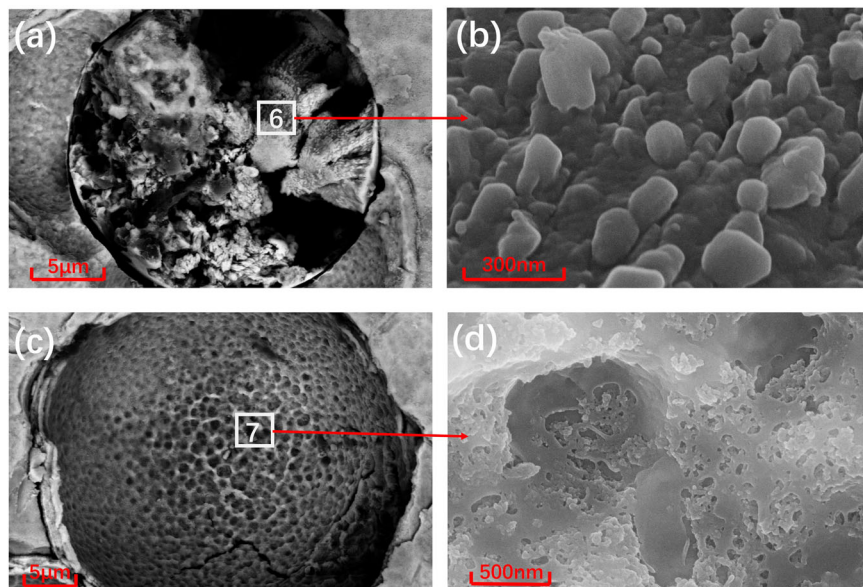


**Fig. 11 SEM images of green glaze corrosion on QHXC-3 surface. a, b** Corrosion pits with irregular internal prominences. **c, d** Corrosion pits with discontinuous corrosion holes inside.

self-excitation, and it postulated that their presence is substantially influenced by the biofilms present on the corroded surface.

In order to determine the origin of self-excited fluorescent substances on the surface<sup>27,28</sup>, a focused analysis was conducted on QHXC-3, which exhibited a single surface corrosion product. Attenuated total reflectance-Fourier transform infrared spectroscopy (ATR-FTIR) was employed for this purpose, with the corrosion area being subjected to further testing, resulting in the infrared spectrum depicted by the red curve in Fig. 15. Notably, in contrast to the characteristic peaks associated with lead carbonate typically generated on the test surface, the ATR-FTIR results unequivocally confirmed the presence of biofilm material on the lead glaze corrosion surface. Meanwhile, the  $-CH_3$  antisymmetric and symmetric stretching vibration peaks were identified at  $2995\text{ cm}^{-1}$  and  $2875\text{ cm}^{-1}$ , whereas the  $-CH_2$  antisymmetric and symmetric stretching vibration peaks were located at  $2915\text{ cm}^{-1}$  and  $2855\text{ cm}^{-1}$ <sup>129</sup>. At  $1369\text{ cm}^{-1}$  is the symmetric vibration of carboxylic acid anion or  $-CH_3$  deformation

vibration, alongside the absorption peak at  $1240\text{ cm}^{-1}$ , corresponding to the stretching vibration peak of C–N. The strong band between  $1150\text{ cm}^{-1}$  and  $1005\text{ cm}^{-1}$  indicated the vibration absorption peak of the C–O–C skeleton<sup>30</sup>. At the same time, in the spectral range of  $1950\text{--}2260\text{ cm}^{-1}$ , a distinct N=C=S stretching vibration peak was observed<sup>31</sup>. This observation suggests the potential existence of metabolic activities associated with microorganisms in the sample.

Due to the prolonged burial of these samples within soil, and in light of the fluorescence distribution, morphological characteristics and infrared functional group test results, it is inferred that these fluorescent substances may have originated from microbial activity. This inference is substantiated by the expected alterations in the pH, dissolved oxygen, ion concentration and organic matter content at the interface between biofilm and cultural relics materials<sup>32</sup>. Microbial metabolism processes, such as the generation of weak acids, including carbonic acid, play a pivotal role in influencing the corrosion behavior of lead glaze<sup>33,34</sup>.  $Pb^{2+}$  on the

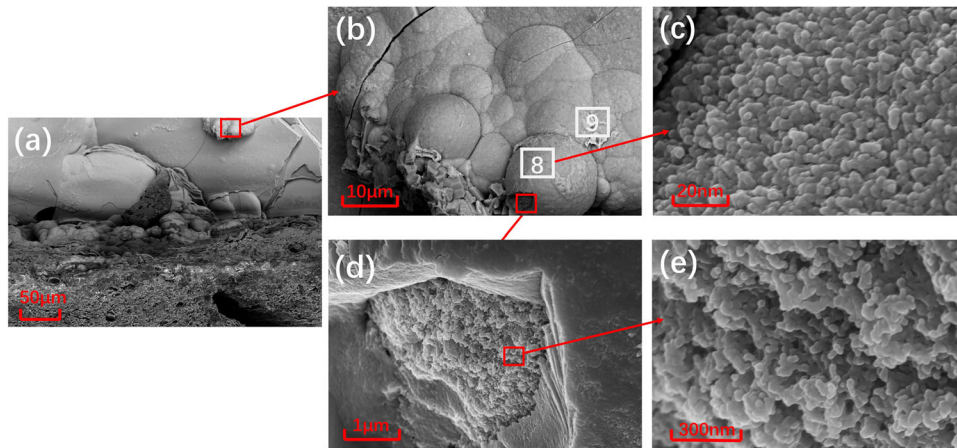


**Fig. 12 SEM images of QHXC-3 glaze cross-section. a, b** Hemispherical adherent deposit of glaze. **c** Surface morphology of the hemispherical adherent deposit. **d, e** Surface topography of the inner subsurface of the hemispherical adherent deposit.

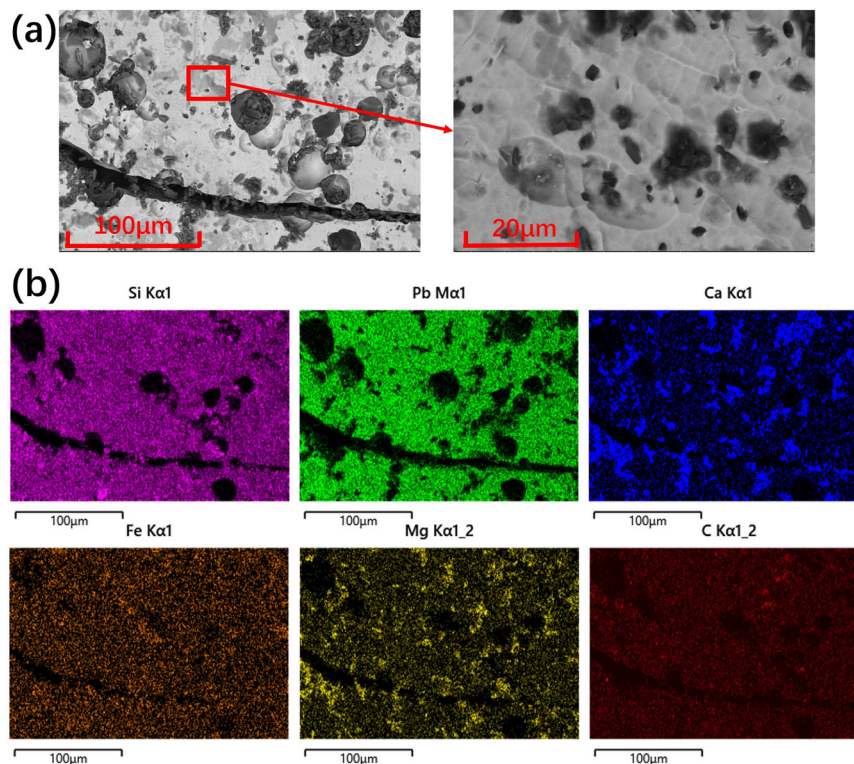


**Fig. 13 SEM-EDX images of QHXC-4 surface. a** Corrosion pits of the glaze. **b** EDX surface scanning images.

glaze surface existed in the form of Si–O–Pb bond and Pb–O–Pb, and the Si–O–Pb structure is susceptible to lead dissolution under the local acidic environment secreted by microorganisms. Consequently, the network structure of  $Pb^{2+}$  in the glaze layer diffuses to the glaze surface, a phenomenon aligned with ion dissolution and precipitation processes. Concurrently, under the action of microorganisms, local corrosion can develop rapidly, resulting in the pitting corrosion of lead glaze and accelerating the corrosion of cracks.

## DISCUSSION

Through the microscopic examination, compositional analysis, and organic matter analysis of the four samples, it becomes evident that QHXC-1, QHXC-2 and QHXC-3 are severely corroded samples.

In contrast, QHXC-4 showcases superior preservation, placing it in the early stages of corrosion. A comparative analysis suggests that in the early stages of corrosion, the glaze surface exhibits the formation of corrosion pits. As these pits extend and deepen, corrosion products develop within some of the more profound corrosion pits. Simultaneously, diverse corrosion products with varied morphologies, such as clusters resembling floral arrangements and petal-like structures, emerge on the surface. These distinct corrosion products accumulate within the glaze, forming semi-spherical deposits. As surface corrosion occurred, various ions and microorganisms from the external burial environment penetrate the glaze interior along cracks, initiating more profound corrosion reactions within these cracks. Due to the anaerobic nature of microorganisms, the crack environment is particularly conducive to their survival. Consequently, in the later stages of



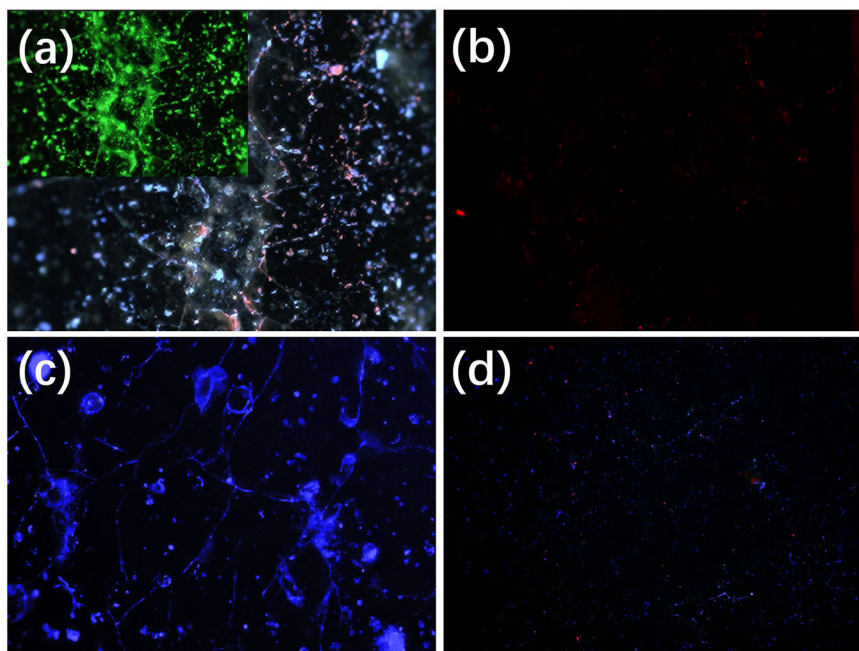


**Fig. 14** Glaze FL images. **a** QHXC-1. **b** QHXC-2. **c** QHXC-3. **d** QHXC-4.

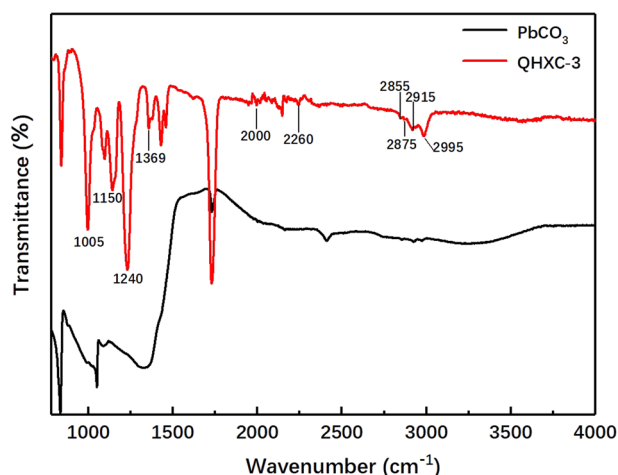


**Fig. 15** Typical ATR-FTIR peaks of lead carbonate and ATR-FTIR test results of QHXC-3.

corrosion, the development of self-exciting fluorescent corrosion ring primarily occurs along glaze cracks, both within these crevices and along their surfaces.

The preceding analysis presents a comparative examination of the corrosion conditions and alterations in composition and structure observed in distinct lead-glazed samples. Based on these findings, it is plausible to postulate that the corrosion mechanism of lead glaze encompasses the following factors:

As illustrated in Fig. 16a, the  $\text{CO}_3^{2-}$  and  $\text{PO}_4^{3-}$  in the buried environment react with the lead or calcium of the glaze, resulting in the formation of calcium carbonate, lead carbonate, lead phosphate and calcium phosphate. Notably, due to the heightened polarization ability of  $\text{Pb}^{2+}$  compared to  $\text{Ca}^{2+}$ ,  $\text{Pb}^{2+}$  exhibits a greater propensity to expedite glaze corrosion through chemical reactions with acidic ions.

As shown in Fig. 16b, the corrosion substances with self-excited fluorescence predominantly reside within the cracks of the glaze. This observation raises the speculation that a substantial

population of microorganisms becomes attached in cracks, consequently resulting in the accumulation of C aggregation in the cracks. Simultaneously, self-excited substances generated in the process of microbial metabolism accumulate in cracks. Additionally, the weak acid produced by microbial metabolism in the crack will react with the ions precipitated from the glaze layer.

Furthermore, the visual representation in Fig. 16c underscores that the products resulting from surface chemical corrosion and microbial corrosion permeated along the cracks of the lead glaze. This process gives rise to an accumulation zone rich in elements such as P and Ca at the interface between the glaze and matrix, and the elements of P and Ca were also enriched and diffused in the matrix.

The three aforementioned corrosion mechanisms are not mutually exclusive. Ions dissolved from the surface of the lead glaze persistently engage in chemical reactions with acid ions in the buried environment, resulting in the continuous formation of carbonates and phosphates. The corrosion products subsequently penetrate into the interior of the lead glaze along the cracks of the lead glaze. Concurrently, the microorganisms attached to the glaze cracks metabolize and generate acidic substances, which in turn react with the glaze layer. This interaction serves to expedite the development of crack corrosion. These corrosion reactions unfold simultaneously and mutually reinforce one another, collectively constituting a comprehensive corrosion system.

Through a comprehensive analysis of corrosion mechanisms, it can be inferred that the corrosion cracks will undergo further expansion. Concurrently, glaze corrosion will persist, advancing in both depth and width dimensions. Given the involvement of microorganisms in the corrosion process, the microbial activity of lead glaze samples upon the excavation is unpredictable. Merely cleaning the corroded areas on the sample surface or controlling preservation conditions may not suffice to completely hinder further corrosion. Hence, simultaneous implementation of a series of sterilization measures during excavation is imperative to ensure the effective and long-term preservation of the samples.

This study involved the comprehensive analysis of four lead-glazed pottery fragments excavated from Xincheng, Xi'an, dating

(a)

glaze

 $\text{Ca}^{2+}$  $\text{Pb}^{2+}$  $\text{CO}_3^{2-}$  $\text{PO}_4^{3-}$  $\text{CaCO}_3$  and  $\text{Ca}_3(\text{PO}_4)_2$  $\text{PbCO}_3$  and  $\text{Pb}_3(\text{PO}_4)_2$ 

$\text{CO}_3^{2-}$  and  $\text{PO}_4^{3-}$  in the soil react chemically with  $\text{Ca}^{2+}$  or  $\text{Pb}^{2+}$  on the surface of the glaze

$\text{Ca}^{2+}$  and  $\text{Pb}^{2+}$  dissolve from inside the glaze

due to the stronger polarization ability of  $\text{Pb}^{2+}$  than  $\text{Ca}^{2+}$ , the chemical reaction produced more  $\text{PbCO}_3$  and  $\text{Pb}_3(\text{PO}_4)_2$  than  $\text{CaCO}_3$  and  $\text{Ca}_3(\text{PO}_4)_2$

(b)

glaze

corrosion products

microorganism

microorganisms accumulate in the cracks of the glaze

self-excited substances produced in the process of microbial metabolism accumulate in cracks.

microorganisms produce weak acid substances which reacted with the glaze layer.

(c)

glaze

pottery matrix

calcium phosphate complex

the products formed of surface chemical corrosion and microbial corrosion permeated along the cracks of the lead glaze

there was an obvious accumulation zone of P and Ca at the interface between the glaze and pottery matrix

P and Ca elements enriched and diffused in the pottery matrix

**Fig. 16 corrosion model. a** Chemical corrosion. **b** Microbial corrosion. **c** Crack corrosion.

back to the Qin and Han Dynasties revealing a multifaceted corrosion process, characterized by several key reactions.

Specifically,  $\text{Ca}^{2+}$  and  $\text{Pb}^{2+}$  dissolved from the surface of the lead glaze underwent chemical reactions, culminating in the formation of  $\text{PbCO}_3$  and  $\text{CaCO}_3$ . Moreover, P present in the soil engaged in reactions with lead or calcium on the glaze surface, resulting in the generation of  $\text{Pb}_3(\text{PO}_4)_2$  and  $\text{Ca}_3(\text{PO}_4)_2$ . Notably, samples exhibiting severe corrosion displayed the presence of self-excited fluorescence substances and organic matter within the cracks of the surface, suggesting the occurrence of microbial corrosion. The acidic substances produced as byproducts of microbial metabolism further accelerated chemical corrosion within these cracks.

The corrosion processes unfolded from the surface towards the interior of the lead glaze, primarily along the glaze layer's cracks. As a consequence, phosphates and microbial metabolites generated during these reactions accumulated within the fissures, forming distinct element-rich accumulation zones rich in P and Ca. These reactions collectively synergized, mutually reinforcing and expediting the overall corrosion of the lead glaze.

Previous research on lead glaze corrosion has predominantly centered around the compositional analysis of corrosion products on sample surfaces. However, this study introduces the concepts of microbial corrosion and crack corrosion in the burial environment. The changes in the mechanisms of corrosion product formation and their alteration processes will necessitate distinct

approaches for the removal of corrosion products in subsequent preservation efforts.

## METHODS

### Analytical techniques

To initiate the determination of the chemical compositions of the samples, four samples underwent examination using XRF (X-ray fluorescence, German Bruker M4 Tornado plus). Prior to testing, each sample was meticulously wiped with anhydrous ethanol. The testing methodology encompassed two distinct approaches: one involving the matrix of the sample, examined via a manual cutting cross-section, and the other involving the glaze, inspected on its natural surface. The instrument uses an X-ray tube featuring a Rh target and adopts the FP method, along with a type correction method employing standard samples (Type-calibration), and uses the quantitative method established by national standard ore sample. The instrument is equipped with a surface scanning mode, and the maximum area of a single surface scan is 190×160 mm<sup>2</sup>.

X-ray diffraction (Germany Bruker D8 discover) analysis was conducted to examine the phase components of the glaze surface with evident surface corrosion. These analyses were directly performed on the natural surface of the samples. The maximum tube pressure of the instrument was 60 kV; the maximum tube current was 80 mA; the optical tube power was 2.2 kW (Cu target), and the angle reproducibility was ±0.0001°. For data collection, a Vantec 500 two-dimensional surface detector with a test spot diameter of 0.5 mm and an integration time of 300 s was utilized.

The examination of the corrosion layer and the well-preserved glaze layer within the most extensively corroded samples was conducted using an American FEI Tecnai G2 F20 field emission transmission electron microscope. These tests were performed on the natural surfaces of the samples without prior pre-treatment, enabling the observation of microscale effects caused by corrosion. The acceleration voltage of the instrument was 200 kV; the point resolution was 0.24 nm, and the line resolution was 0.14 nm; the STEM (HAADF) resolution was 0.19 nm, and the electron beam energy dispersion was less than 0.7 eV.

Field emission scanning electron microscopy equipped with energy dispersive X-ray spectroscopy (FEI Verios G4) was used to observe the microscopic morphologies of the surface and cross-sections of the two samples exhibiting the most severe corrosion and one well-preserved sample, along with compositional analysis. In the preparation of the test samples, the cross-sections were meticulously cut and polished, with no prior treatment applied to the etched surface. Prior to testing, the entire sample underwent ultrasonic cleaning using anhydrous ethanol and ion sputtering instrument chromium plating. During testing, the voltage was set to 10 kV, and the working distance varied from 4.0 to 6.4 mm under vacuum conditions. The test results included secondary electron images and backscattered electron images.

To assess the presence of bioluminescence on the samples, the surface corrosion layer was examined using an inverted fluorescence phase contrast microscope (Japanese Keyence BZ-X800E). This analysis was carried out directly on the natural surfaces of the samples. The microscope was equipped with three different filters, namely DAPI-V, GFP, and TRITC, and utilized a transmission light source of 3.7 W, complemented by a 40 W fluorescent fall-out light source.

In addition, an attenuated total reflectance-Fourier infrared spectrometer (American PerkinElmer Spotlight400) was employed to investigate the samples exhibiting strong fluorescence reactions. This allowed for the analysis of functional groups within the corrosion material and the determination of the presence of microbial corrosion. Infrared absorption spectroscopy was conducted on the corrosion area of the samples without any pre-

treatment. The spectral range examined spanned from 500–4000 cm<sup>-1</sup> with a spectral resolution exceeding 0.09 cm<sup>-1</sup>, and the wavenumber accuracy better than 0.01 cm<sup>-1</sup>.

### DATA AVAILABILITY

The datasets generated during and/or analyzed during the current study are available from the corresponding author on reasonable request.

Received: 25 September 2023; Accepted: 4 January 2024;

Published online: 18 January 2024

### REFERENCES

- Tite, M., Shortland, A. & Paynter, S. The beginnings of vitreous materials in the near East and Egypt. *Acc. Chem. Res.* **35**, 585–593 (2002).
- Vandiver, P. Glass technology at the mid-second-millennium B.C. Hurrian Site of Nuzi. *J. Glass Stud.* **25**, 239–247 (1983).
- Cohen, D. J., Bar-Yosef, O., Wu, X., Patania, I. & Goldberg, P. The emergence of pottery in China: Recent dating of two early pottery cave sites in South China. *Quat. Int.* **441**, 36–48 (2017).
- Chen, Y. L., Wen, R. & Wang, T. Y. The origins of low-fire polychrome glazed pottery in China. *Antiquity*. **94**, E30–E30 (2020).
- Dong, J., Li, Q. & Liu, S. Scientific analysis of some glazed pottery unearthed from Warring States Chu tombs in Jiangling, Hubei Province: Indication for the origin of the low-fired glazed pottery in China. *X-Ray Spectrom.* **49**, 5 (2020).
- Gan, F., Cheng, H. & Li, Q. Origin of Chinese ancient glasses—study on the earliest Chinese ancient glasses. *Sci. China Ser. E: Technol. Sci.* **49**, 6 (2006).
- Bette, S., Eggert, G., Fischer, A., Stelzner, J. & Dinnebieber, R. E. Characterization of a new efflorescence salt on calcareous historic objects stored in wood cabinets: Ca<sub>2</sub>(CHCOO)(HCOO)(NO<sub>3</sub>)<sub>2</sub>·4H<sub>2</sub>O. *Corrosion Sci.* **132**, 68–78 (2018).
- Liang, P., Yang, X. & Wu, L. Reflection properties of the ‘silvery glaze’ on the green glaze of Chinese traditional potteries. *J. Opt. A: Pure Appl. Opt.* **10**, 11 (2008).
- Li, Z., Ma, Y., Ma, Q., Chen, J. & Song, Y. New perspective on Jun glaze corrosion: study on the corrosion of light greenish blue and reddish purple glazes from Juntai Kiln, Yuzhou, Henan, China. *Herit. Science* **8**, 1 (2020).
- Gin, S. et al. Origin and consequences of silicate glass passivation by surface layers. *Nat. Commun.* **6**, 6360 (2015).
- Palomar, T., Chabas, A., Bastidas, D. M., de la Fuente, D. & Verney-Carron, A. Effect of marine aerosols on the alteration of silicate glasses. *J. Non-Cryst. Solids* **471**, 328–337 (2017).
- Bunker, B. C. Molecular mechanisms for corrosion of silica and silicate glasses. *J. Non-Cryst. Solids* **179**, 300–308 (1994).
- Tournie, A., Ricciardi, P. & Colomban, P. Glass corrosion mechanisms: a multiscale analysis. *Solid State Ion.* **179**, 38 (2008).
- Bette, S., Eggert, G., Fischer, A. & Dinnebieber, R. E. Glass-induced lead corrosion of heritage objects: structural characterization of KOH-2PbCO<sub>3</sub>. *Inorg. Chem.* **56**, 10 (2017).
- Liu, S., Li, Q. H., Gan, F., Zhang, P. & Lankton, J. W. Silk road glass in Xinjiang, China: chemical compositional analysis and interpretation using a high-resolution portable XRF spectrometer. *J. Archaeol. Sci.* **39**, 7 (2012).
- Yin, X., Huang, T. & Gong, H. Chemical evolution of lead in ancient artifacts—A case study of early Chinese lead-silicate glaze. *J. Eur. Ceram. Soc.* **40**, 54 (2020).
- Zhu, T. et al. Analysis on the “silvery glaze” of green glazed pottery of song dynasty and its formation mechanism. *Chin. J. Chem.* **24**, 9 (2007).
- Zhu, T., Wang, C., Mao, Z., Li, L. & Huang, H. Identification of different corrosion covering the surface of Chinese ancient lead glazed potteries. *Spectrosc. Spectr. Anal.* **30**, 1 (2010).
- Arena, H. et al. Impact of iron and magnesium on glass alteration: Characterization of the secondary phases and determination of their solubility constants. *Appl. Geochem.* **82**, 119–133 (2017).
- Yin, X., Huang, T. & Gong, H. Chemical evolution of lead in ancient artifacts: a case study of early Chinese lead-silicate glaze. *J. Eur. Ceram. Soc.* **40**, 54 (2020).
- Michelin, A. et al. Silicate glass alteration enhanced by iron: origin and long-term implications. *Environ. Sci. Technol.* **47**, 2 (2013).
- Weaver, J. L. et al. Microbial interactions with silicate glasses. *NPJ Mater. Degrad.* **5**, 1 (2021).
- Aulinas, M. et al. Weathering patinas on the medieval (S. XIV) stained glass windows of the Pedralbes Monastery (Barcelona, Spain). *Environ. Sci. Pollut. Res.* **16**, 4 (2009).
- Rodrigues, A. et al. Fungal biodeterioration of stained-glass windows. *Int. Biodeterior. Biodegrad.* **90**, 152–160 (2014).

25. Branysova, T., Demnerova, K., Durovic, M. & Stiborova, H. Microbial biodeterioration of cultural heritage and identification of the active agents over the last two decades. *J. Cult. Herit.* **55**, 245–260 (2022).
26. Lin, Z., Li, M. & Zhou, Y. TEM investigations on layered ternary ceramics. *J. Mater. Sci. Technol.* **23**, 2 (2007).
27. Tian, Y. et al. Advances in detection of microorganisms using near-infrared spectroscopy. *Anal. Methods.* **13**, 23 (2021).
28. Lu, X., Al-Qadiri, H. M., Lin, M. & Rasco, B. A. Application of Mid-infrared and Raman Spectroscopy to the Study of Bacteria. *Food Bioprocess Technol.* **4**, 6 (2011).
29. Brownson, J. R. S., Tejedor-Tejedor, M. I. & Anderson, M. A. FTIR spectroscopy of alcohol and formate interactions with mesoporous TiO<sub>2</sub> surfaces. *J. Phys. Chem. B.* **110**, 12494–12499 (2006).
30. Rao, L. S., Naidu, C. D. & Tiwari, S. Investigation on synthesis, structure and degradability of starch based bioplastics. *Mater. Today.* **49**, 257–261 (2022).
31. Ellison, M. D. & Hamers, R. J. Adsorption of phenyl isothiocyanate on Si(001): A 1,2-dipolar surface addition reaction. *J. Phys. Chem. B.* **103**, 6243–6251 (1999).
32. Wang, J., Li, X. & Wang, W. The effect of microorganism attachment on the Open-circuit-potential of passive metals in seawater. *J. Chin. Soc. Corros. Prot.* **5**, 7–11 (2004).
33. Salek, S. S., Bozkurt, O. D., van Turnhout, A. G., Kleerebezem, R. & van Loosdrecht, M. C. M. Kinetics of CaCO<sub>3</sub> precipitation in an anaerobic digestion process integrated with silicate minerals. *Ecol. Eng.* **86**, 105–112 (2016).
34. Wu, Y. et al. Genome and transcriptome analysis of rock-dissolving *Pseudomonas* sp. NLX-4 strain. *Bioresour. Bioprocess.* **9**, 1 (2022).

## ACKNOWLEDGEMENTS

This work was supported by the National Natural Science Foundation of Shanghai in China [20ZR1422800] and the Key Program of the National Natural Science Foundation of China [51732008].

## AUTHOR CONTRIBUTIONS

K.Z. and W.Y. carried out the experiments and wrote the first draft manuscript, C.W. provided experimental samples, J.Z. designed the experiments and performed the

analyses, M.Z. performed the analyses. All co-authors discussed the results and commented on the manuscript. All authors reviewed, edited the final manuscript. All authors read and approved the final manuscript.

## COMPETING INTERESTS

The authors declare no competing interests.

## ADDITIONAL INFORMATION

**Correspondence** and requests for materials should be addressed to Chen Wu or Jing Zhao.

**Reprints and permission information** is available at <http://www.nature.com/reprints>

**Publisher's note** Springer Nature remains neutral with regard to jurisdictional claims in published maps and institutional affiliations.



**Open Access** This article is licensed under a Creative Commons Attribution 4.0 International License, which permits use, sharing, adaptation, distribution and reproduction in any medium or format, as long as you give appropriate credit to the original author(s) and the source, provide a link to the Creative Commons license, and indicate if changes were made. The images or other third party material in this article are included in the article's Creative Commons license, unless indicated otherwise in a credit line to the material. If material is not included in the article's Creative Commons license and your intended use is not permitted by statutory regulation or exceeds the permitted use, you will need to obtain permission directly from the copyright holder. To view a copy of this license, visit <http://creativecommons.org/licenses/by/4.0/>.

© The Author(s) 2024